The Areal Reduction Factor: A Multifractal Analysis

By
Daniele Veneziano and Andreas Langousis

Department of Civil and Environmental Engineering, MIT, Cambridge, Mass., USA

Submitted to
Water Resources Research

March, 2005

---

*Corresponding author: Daniele Veneziano, Dept. of Civil and Environmental Engineering, MIT, Cambridge, Mass. 02139. Tel: 617-253-7199, venezian@mit.edu.

Abstract

The areal reduction factor (ARF) η is a key quantity in the design against hydrologic extremes. For a basin of area a and a duration d, $\eta(a, d, T)$ is the ratio between the average rainfall intensity in a and d with return period T and the average rainfall intensity at a point for the same d and T. Empirical ARF charts often display scaling behavior. For example, for large $(\sqrt{a}/d)$ ratios and given T, the ARF tends to behave like $(\sqrt{a}/d)^{-\alpha}$ for some α. Here we obtain scaling properties of the ARF under the condition that space-time rainfall has multifractal scale invariance. The scaling exponents of the ARF are related in a simple way to the multifractal properties of the parent rainfall process. We consider regular and highly elongated basins, quantify the effect of rainfall advection, and investigate the bias from estimating the ARF using sparse raingauge networks. We also study the effects of departure of rainfall from exact multifractality. The results explain many features of empirical ARF charts while suggesting dependencies on advection, basin shape, and return period that are difficult to quantify empirically. The theoretical scaling relations may be used to extrapolate the ARF beyond the empirical range of a, d and T.

Index Terms

1833 Hydroclimatology; 1854 Precipitation (3354); 1869 Stochastic processes; 3250 Fractals and multifractals

Keywords

Rainfall extremes, areal reduction factor, intensity duration frequency curves, scale invariance, multifractal processes

1. Introduction

In hydrological risk analysis and design, one is often interested in the rainfall intensity averaged over a region of area a and duration d, with return period T. Plotting such extreme rainfall intensity $I(a, d, T)$ against d for given a and T produces so-called Intensity Duration Area Frequency (IDAF) curves. For $a \to 0$ (precipitation at a point), the IDAF curves reduce to the familiar Intensity Duration Frequency (IDF) curves; see for example Singh (1992), p. 905-908. While various definitions of T are in use, the one that makes best sense for many hydrologic applications and is easiest to handle analytically is the reciprocal of the exceedance rate (e.g. Willems, 2000; Veneziano and Furcolo, 2002a). Accordingly, $I(a, d, T)$ is the intensity i that satisfies

$$P[I(a, d) > i] = \frac{d}{T} \tag{1}$$

where $I(a, d)$ is the average intensity in $(t, t + d)$.

Direct estimation of the IDAF curves from rainfall data requires very long records from spatially dense raingauge networks or radar, which are seldom available. A common strategy to avoid direct estimation is to express $I(a, d, T)$ as the product of the IDF value $I(d, T)$ and the areal reduction factor (ARF) $\eta(a, d, T) = \frac{I(a, d, T)}{I(d, T)}$. Advantages of this factored approach are that the IDF values can be found using long records from single pluviometric stations (which are available at many locations) and, if the ARF does not vary much in space, the function $\eta(a, d, T)$ needs be estimated just once. In the literature, two different types of ARFs are found: the storm centered ARF and the fixed area ARF (Hershfield, 1962; Omolayo, 1993). The storm centered ARF is associated with rainfall intensity within the isohyets of specific storm events, and does not have a precise return-period interpretation. By contrast the fixed area ARF is obtained as the ratio of return-period rainfall intensities over a fixed area and at a point. Hence the fixed-area definition of the ARF is better suited for hydrologic risk analysis, and is the one used throughout this paper.

General properties of empirical $\eta(a, d, T)$ functions are that (1) η increases as a decreases or d increases approaching unity as $a \to 0$ or $d \to \infty$ and (2) for large a and small d, η depends on a and d through $\sqrt{a}/d$; see NERC (1975) Vol. II, p. 40. Whether and how η depends on the return period T is less clear. NERC (1975) reports a weak dependence, whereas Bell (1976), Asquith and Famiglietti (2000), and De Michele *et al.* (2001) found that η decreases significantly as T increases. ARF charts for routine hydrologic design (e.g. Leclerc and Schaake, 1972; NERC, 1975; Koutsoyiannis, 1997) typically give η as a function of only a and d.

An alternative to empirical IDF, IDAF and ARF estimation is to use theoretical analysis based on a random-process representation of rainfall. Some studies have derived properties of the IDAF curves and the ARFs using non-scaling representations of rainfall. An early attempt in this direction was made by Roche (1966) who developed a theoretical approach to point and areal rainfall based on the correlation structure of intense storms. Rodriguez-Iturbe and Mejia (1974) extended Roche's (1966) approach by assuming that the rainfall field is a zero mean stationary Gaussian process. A different approach to ARF estimation, based on crossing properties of random fields, was proposed by Bacchi and Ranzi (1996). . Properties of extremes of random functions were used also by Sivapalan and Blöschl (1998). Finally, Asquith and Famiglietti (2000) derived the ARF as the catchment average of the ratio between the T-year rainfall depths at distance r from the centroid of the storm and at the centroid itself.

Several other studies have assumed that rainfall intensity has scale invariance and used multifractal analysis to derive scaling properties of the IDF curves and ARFs with a, d and T. De

Michele *et al.* (2001) have argued directly that the annual maximum value of $I(d, a)$ could scale in a self similar or multifractal way with d and a. They then focus on the self similar case and specify the form of $I(a, d, T)$ by reasoning on the limiting behavior when $a \rightarrow 0$ and a or $d \rightarrow \infty$. By contrast, Hubert *et al*. (1998) and Veneziano and Furcolo (2002a) derive scaling properties of the IDF curves with d and T from the condition that rainfall has multifractal scale invariance. In a recent study, Castro *et al*. (2004) developed a multiftractal approach to explain how the IDAF values scale with a, d and T. Although not explicitly stated, the analysis of Castro *et al*. (2004) is valid only for large values of T; see Langousis (2004).

Multifractal models are attractive for studying rainfall scaling since they provide parsimonious representations of space-time rainfall fields (Lovejoy and Schertzer, 1995; Gupta and Waymire, 1993; Deidda, 2000), and possess scaling properties that likely determine the power-law behaviors of empirical IDF, IDAF curves and ARFs. However, several studies (e.g. Fraedrich and Larnder, 1993; Olsson *et al.*, 1993; Olsson, 1995; Menabde *et al*., 1997) have shown that temporal rainfall ceases to be multifractal for aggregation periods larger than about 2 weeks or smaller than several minutes. Also the analysis of rainfall fields in space and space-time reveals systematic deviations from exact multifractality (Veneziano *et al*., 2005).

In this paper, we study the behavior of the IDAF curves and the areal reduction factor η under exact and approximate multifractality. We also analyze how these quantities depend on basin shape and rainfall advection and quantify the distortions in ARF scaling caused by the common practice of estimating area rainfall from sparse pluviometric networks. Finally, we show how the theoretical results explain many features of empirical ARFs.

Since in certain limiting cases to be considered later (such as sampling along a line segment) the basin has finite extent but zero area, it is convenient to parameterize the basin through its shape S and largest linear dimension l rather than area a. For example, a basin could have in approximation the shape S of a disc, a square or a rectangle with a given aspect ratio. Together, S and l define the planar geometry of the basin (except for rigid translation, rotation, or reflection). Accordingly, we use the notation $I(S, l, d, T)$ and $\eta(S, l, d, T)$ in place of the less descriptive $I(a, d, T)$ and $\eta(a, d, T)$.

In hydrologic applications, the averaging duration d is often related to the response time of the basin, for example the concentration time, but in general the region of interest needs not be a river basin and d needs not refer to the travel time of water particles. While hydrologic extremes remain the main practical focus of our analysis and consequently we refer to the geographical region as a “basin”, results hold beyond this application context.

2. IDAF and ARF Scaling under Multifractal Rainfall

Veneziano and Furcolo (2002a) analyzed the IDF curves when temporal rainfall is a stationary multifractal process. Multifractality means that, for any given duration d and scaling factor $r \geq 1$,

$$I(t|d) \overset{\mathrm{d}}{=} B_r\, I(rt|rd) \tag{2}$$

where $I(t|d)$ is the mean rainfall intensity in $[t, t + d]$, B_r is a non-negative random variable with mean value 1 whose distribution depends on r, and $\overset{\mathrm{d}}{=}$ denotes equality of all n-dimensional distributions (statistical equivalence of the two processes); see for example Gupta and Waymire (1990) or Veneziano (1999). The distribution of B_r, which determines the scaling properties of the rainfall process, can be characterized by the moment-scaling function $K(q) = \log_r(E[B_r^q])$. For example, if B_r has lognormal distribution, then $K(q) = C_1(q^2 - q)$ where $C_1 = \frac{1}{2}\mathrm{Var}[\log_r(B_r)]$ is a parameter. Equation (2) expresses the property of multifractal scale invariance. Due to stationarity, $I(t|d)$ is also invariant with respect to shifts of the time parameter.

Hubert *et al*. (1998) and Veneziano and Furcolo (2002a) found that, under equation (2), the IDF function $I(d, T)$ has the following asymptotic properties:

$$I(d, T) \propto \begin{cases} d^{-\gamma_1} T^{\frac{1}{q_1}}, & \text{for any finite } T \text{ and } d \to 0 \\ d^{-1} T^{\frac{1}{q_1^*}}, & \text{for any finite } d \text{ and } T \to \infty \end{cases} \tag{3}$$

The constants γ_1, q_1 and q_1* in equation (3) can be found from the function $K(q)$ as shown in Figure 1: γ_1 is the slope of the tangent to $K(q)$ with Y-intercept equal to –1, q_1 is the value of q at the point of tangency, and q_1* is the order above which the moments of $I(t|d)$ diverge (q_1* can be found as the value of $q > 1$ such that $K(q) = q - 1$). For example, in the case of a lognormal multifractal process with parameter C_1, these constants are $\gamma_1 = 2\sqrt{C_1} - C_1$, $q_1 = 1/\sqrt{C_1}$, and $q_1^* = 1/C_1$.

Next we extend the analysis of Veneziano and Furcolo (2002a) from point to spatially averaged rainfall. While the extension is in many ways straightforward, new elements to be considered are that the scaling of the IDAF values depends on the linear size l and shape S of the basin and the rainfall advection velocity v_{ad}.

2.1 Lagrangian Scaling of Multifractal Space-time Rainfall

The case of no advection corresponds to working in a Lagrangian reference that moves with the rainfall field. In that reference, rainfall is assumed to be a stationary random measure with isotropic multifractality in space and time. In analogy with equation (2), this means that for any basin (S, l), duration d and scaling factor $r \geq 1$,

$$I(t|S, l, d) \overset{d}{=} B_r\, I(rt|S, rl, rd) \tag{4}$$

where $I(t|S, l, d)$ is the mean rainfall intensity inside the basin (S, l) during $[t, t + d]$ and all other notation is as in equation (2).

Multifractal scaling applies below some maximum region size l_{max} and duration d_{max}, which might represent the size and duration of the largest organized rainfall features at the synoptic scale. It is then convenient to use l_{max} and d_{max} to render all length and time variables dimensionless. For example, $L = l/l_{max}$ and $D = d/d_{max}$ are the dimensionless basin size and averaging duration. When using such dimensionless quantities, equation (4) becomes

$$I(t|S, L, D) \overset{d}{=} B_r\, I(rt|S, rL, rD) \tag{5}$$

To further discuss the scaling properties of space-time rainfall, we introduce two quantities with the physical dimension of velocity [length/time]. One is the "rainfall evolution rate" $v_{rain} = l_{rain}/d_{rain}$, where l_{rain} and d_{rain} are the linear size and lifetime of organized rainfall features such as convective cells, cell clusters or mesoscale precipitation regions. For what follows, it is not important to specify which of these features l_{rain} and d_{rain} refer to, because what matters is the ratio $v_{rain} = l_{rain}/d_{rain}$ and, under isotropic multifractality, v_{rain} is the same for all such features. In particular, $v_{rain} = l_{max}/d_{max}$.

The other quantity is the "response velocity" $v_{res} = l/d$, where l and d are the maximum linear size of the basin and the duration of rainfall averaging (as stated in the Introduction, d is a duration of interest, which may or may not correspond to the hydrologic response time of the basin). What matters for the analysis that follows is the relative magnitude of v_{rain} and v_{res}, as expressed by the dimensionless "response velocity parameter" $u_{res} = v_{res}/v_{rain} = \dfrac{l/d}{l_{max}/d_{max}} = \dfrac{l/l_{max}}{d/d_{max}} = L/D$, where L and D are the normalized quantities introduced above. The parameter u_{res} indicates whether the response of the basin is faster ($u_{res} > 1$) or slower ($u_{res} < 1$) than the evolution rate of the rainfall features. For example, if d is set equal to the concentration time of the basin (on the concentration time, see for example Viessman and Lewis (2003), p. 265), then v_{res} ranges approximately between 3 and 8 Km/h depending mainly on the average slope of the basin; for a detailed analysis see Langousis (2004). On the other hand, the rainfall evolution rate v_{rain} ranges from about 5 to 20 Km/h; see for example Austin and Houze (1972), Orlanski (1975) and the review in Langousis (2004). Hence u_{res} may be either smaller or larger than 1.

We now return to the multifractal scaling property in equation (5). That property can be represented graphically by noting that rainfall intensity has "B_r multifractal scaling" along 45^o lines on the [ln(L), ln(D)] plane; see Figure 2a. Each 45^o line in Figure 2a is characterized by one value of the response velocity parameter $u_{res} = L/D$. The line with $u_{res} = 1$, denoted by U_1, corresponds to square regions on the (L, D) plane and has special importance. Below U_1 is the "fast response region" where $u_{res} > 1$ and above U_1 is the "slow response region" where $u_{res} < 1$. The regions where $u_{res} >> 1$ (in practice, u_{res} larger than about 5) and $u_{res} << 1$ (u_{res} smaller than about 1/5) will be referred to as the very fast and very slow response regions, respectively. In Figure 2, we have made use of rectangles with side lengths L and D to visually illustrate the relative value of these quantities and conditions when $u_{res} = L/D$ is smaller or larger than 1.

Multifractality is expressed by the scale invariance property in equation (5). It is important to notice that in the right hand side of that equation L and D are stretched by the same factor r (hence also the physical length $l = Ll_{max}$ and physical averaging duration $d = Dd_{max}$ are both stretched by r). However, more general scaling relations hold in good approximation in the very fast and very slow response regions. When $u_{res} >> 1$, the temporal process $I(rt|S, rL, rD)$ in equation (5) is insensitive to D, provided that D remains much smaller than L (see Veneziano and Furcolo, 2002b). The basic reason is that for $D << L$ the temporal correlation of rainfall intensity within an interval of duration $d = Dd_{max}$ is much closer to 1 than the spatial correlation along a spatial segment of length $l = Ll_{max}$. Using this property and equation (5), one obtains

$$I(t|S, L, D) \overset{d}{=} B_{r_L}\, I(r_L t|S, r_L L, r_D D)\ ,\ \ r_L \geq 1;\ \ u_{res} >> 1 \tag{6}$$

The scaling factor r_D in equation (6) is arbitrary, provided that $(r_L L)/(r_D D) >> 1$.

For $u_{res} << 1$, L is much smaller than D and a similar argument gives the following scaling relation, which is symmetrical to equation (6):

$$I(t|S, L, D) \stackrel{d}{=} B_{r_D} I(r_D t|S, r_L L, r_D D) \ , \ r_D \geq 1; \ u_{res} << 1 \tag{7}$$

In this case r_L is arbitrary, provided that $(r_L L)/(r_D D) << 1$.

The scaling relations in equations (6) and (7) are shown schematically in Figure 2b**.** What is given along each arrow in the figure is the scaling factor in each transformation of L and D ("1" means that the distribution is unchanged by the transformation). For example, raingauge records have minimal area coverage; hence scaling in time is of the B_{r_D} multifractal type, as given by equation (7) and shown at the top left of Figure 2b. In the region around the U_1 line (for u_{res} in the approximate range [1/5, 5]), equations (6) and (7) do not apply. Rather, there are complicated transformations $T_{D,r}$ and $T_{L,r}$ in the directions of the log(D) and log(L) axes, which in combination produce B_r multifractal scaling along 45-degree lines; see dashed triangle in Figure 2b.

Next we derive the scaling properties of the IDAF curves and ARFs in the very fast and very slow response regions. We start with two limiting basin shapes, a square (or disc) and a line segment, and then discuss the case of general rectangular regions. Section 2.2 assumes no advection and Section 2.3 extends the results to $v_{ad} \neq 0$.

2.2 IDAF and ARF Scaling: No Rainfall Advection

In the very slow response region equation (7) holds and recalling equation (3) one finds that, for basins of given shape S,

$$I(S, L, D, T) \propto \begin{cases} D^{-\gamma_1}\, T^{\frac{1}{q_1}} & \text{, for } T \text{ finite and } D \to 0 \\ D^{-1}\, T^{\frac{1}{q_n*}} & \text{, for } D \text{ finite and } T \to \infty \end{cases} \quad , \; u_{res} << 1 \tag{8}$$

Notice that equation (3) holds for temporal rainfall (in this case the Euclidean space dimension is $n = 1$ and the critical moment order is q_1*), whereas equation (8) is for space-time regions of any Euclidean dimension n (e.g. $n = 2$ if rainfall is observed along a line segment and $n = 3$ if rainfall is observed inside a region with positive area). In the latter case, the order of moment divergence q_n* is the value of $q > 1$ such that $K(q) = n(q - 1)$; see Figure 1. For example, in the case of lognormal multifractal rainfall, $q_n* = n/C_1$. The reason why the right hand side of equation (8) does not contain L is that, for $u_{res} << 1$, I is insensitive to the size of the basin.

In the very fast response region equation (6) holds and, in analogy with equation (8),

$$I(S, L, D, T) \propto \begin{cases} L^{-\gamma_1}\, T^{\frac{1}{q_1}} & \text{, for } T \text{ finite and } L \to 0 \\ L^{-1}\, T^{\frac{1}{q_n*}} & \text{, for } L \text{ finite and } T \to \infty \end{cases} \quad , \; u_{res} >> 1 \tag{9}$$

In this case, I is insensitive to the averaging duration. Equations (8) and (9) give asymptotic scaling properties for the IDAF values. Next we use these properties and the time-only results in equation (3) to derive scaling relations for $\eta(\mathrm{S}, L, D, T) = \dfrac{I(S, L, D, T)}{I(D, T)}$.

In the very slow response region (for L/D small), equations (3) and (8) give

$$\eta(\mathrm{S}, L, D, T) = \begin{cases} \approx 1 & \text{, for } T \text{ finite and } D \to 0 \\ \propto T^{\left(\frac{1}{q_n*} - \frac{1}{q_1*}\right)} & \text{, for } D \text{ finite and } T \to \infty \end{cases} \quad , \qquad u_{res} << 1 \tag{10}$$

whereas in the very fast response region (for L/D large), equations (3) and (9) give

$$\eta(S, L, D, T) \propto \begin{cases} \left(\frac{L}{D}\right)^{-\gamma_1} & \text{, for } T \text{ finite and } L \to 0 \\ & , \qquad u_{res} >> 1 \\ \left(\frac{L}{D}\right)^{-1} T^{\left(\frac{1}{q_n^*} - \frac{1}{q_1^*}\right)} & \text{, for } L \text{ finite and } T \to \infty \end{cases} \tag{11}$$

Equations (10) and (11) show that η depends on the response velocity L/D, the return period T and, through n in q_n*, the shape of the observation region. Notice that, when the response velocity parameter $u_{res} = L/D$ is small, the ARF does not depend on L and D and is close to 1. If on the other hand u_{res} is high, the ARF becomes a power function of L/D, whose exponent depends on T. These properties correspond to features typically observed in empirical ARFs; see for example NERC (1975), Koutsoyiannis (1997), Asquith and Famiglietti (2000), and De Michele *et al.* (2001).

Before we include advection, we briefly mention two issues related to the algebraic tail of the rainfall intensity distribution and its implications on how η behaves for large T. Consider a generic rectangular space-time region (L_1xL_2xD) with $L_1 \geq L_2$. If rainfall is a fully developed multifractal process and $q_3^* < \infty$, then for $L_2 > 0$ the marginal distribution of $I(t|L_1, L_2, D)$ has a "q_3* upper tail" of the type $P[I(t|L_1, L_2, D) > i] \sim i^{-q_3^*}$. Hence the asymptotic scaling results for square regions [n = 3 in equations (8)-(11)] hold also for general rectangular regions. However, the upper tail of the average rainfall intensity in a rectangular region may include first a range with algebraic q_1* behavior, followed by a range with q_2* behavior and finally by the extreme q_3* tail, as illustrated in Figure 3. A limited q_1* tail develops if one of the three dimensions (L_1, L_2, or D) clearly dominates over the other two and a limited q_2* tail develops if one of the three dimensions is much smaller than the other two. For example, a sequence of q_1*, q_2*, and q_3* tail regimes exists if $L_1 >> L_2 >> D$. Similar considerations apply when observing rainfall on a line segment. In this case, if $L >> D$ or $L << D$, there is a non-extreme q_1* tail that precedes the extreme q_2* tail.

The second issue is that fully-developed multifractal processes like those we have considered up to now have singularities that cannot exist in nature. The singularities are due to oscillations at sub-observation scales which, when continued to infinite resolution, cause divergence of the moments of $I(t|S, L, D)$ of order $q \geq q_n*$. More plausible models of rainfall are multiplicative cascades developed to a finite resolution or, as we shall consider later, "bounded" cascades in which the fluctuations at finer scales have decreasing amplitudes (Menabde *et al.*, 1997). In either case, the distribution of $I(t|S, L, D)$ does not have an algebraic upper tail and for $T \to \infty$ the IDAF and ARF values do not have (an exact) power-law dependence on T.

The main conclusion from these considerations is that the scaling relation $\eta \propto T^{\left(\frac{1}{q_n*} - \frac{1}{q_1*}\right)}$ with $n > 1$, which is predicted by theory for $T \to \infty$, may not apply in reality or may occur for return periods that are too large to be of practical interest.

2.3 The Effect of Advection

To our knowledge, the effect of rainfall advection on the IDAF curves and the ARF values has not been previously studied. This effect largely depends on the "advection velocity parameter" u_{ad}, defined as the dimensionless ratio $u_{ad} = v_{ad}/v_{rain}$ between the advection velocity v_{ad} and the rainfall evolution rate v_{rain}. As before, we assume that in a Lagrangian reference that tracks the rainfall motion, rainfall intensity satisfies the multifractal scale invariance condition in equation (5). To determine the effect of v_{ad} on the IDAF and ARF values, one must find how advection changes the shape and size of the rainfall averaging regions from a Eulerian (fixed) to a Lagrangian (moving) reference frame and then use results from Section 2.2 for the Lagrangian regions. Here we do so for rainfall observed at a geographical point, along a line segment, or over a disc. Primed symbols denote quantities in the Lagrangian reference. We work with dimensionless length L and duration D, but analogous relations hold for the un-normalized quantities l and d.

(a) Observation of Rainfall at a Point

As shown in Figure 4a, when averaging advected rain during a period D, the averaging segment in the Lagrangian reference has length $D' = \sqrt{D^2 + D^2 (u_{ad})^2} = D \sqrt{1+ u_{ad}^2}$. Next we will show that the Lagrangian return period T' that corresponds to the Eulerian T is $T' = T\sqrt{1+ u_{ad}^2}$.

Consider rainfall intensity at a fixed geographical point, averaged in an interval of duration d. In T units of time, there are $n = T/d$ such intervals; hence $I(d, T)$ is the intensity i such that $P[I(d) > i] = 1/n = d/T$. In the case when $u_{ad} > 0$, $I(d)$ is the average of the Lagrangian rainfall intensity field over a segment of length $d' = d\sqrt{(1+u_{ad}^2)}$ (see Figure 4a). In T units of time, the sampling point in the Lagrangian reference covers a segment of length $T' = nd' = \frac{Td'}{d}$ $= T\sqrt{(1+u_{ad}^2)}$. Therefore, $I(d, T\,|u_{ad}) = I(d\sqrt{(1+u_{ad}^2)}, T\sqrt{(1+u_{ad}^2)}\,|u_{ad} = 0)$.

As a consequence of this analysis, if for $u_{ad} = 0$ the IDF value varies with D and T as $D^{-\alpha}\,T^{\beta}$, then for $u_{ad} \neq 0$ the IDF values must be multiplied by $(1+u_{ad}^2)^{½(\beta-\alpha)}$. Since $\alpha > \beta$ (see equation (3)), this factor is smaller than 1.

(b) Averaging Rainfall along a Line Segment

Suppose now that rainfall is observed along a line segment of length L parallel to the y-axis during a period D. In this case the Lagrangian space-time averaging region is a parallelogram with side lengths $L' = L$ and $D' = D\sqrt{1+ u_{ad}^2}$; see Figure 4b. The Lagrangian return period is $T' = T\sqrt{1+ u_{ad}^2}$, as in the case of sampling at a point. To understand the implications of these transformations on the IDAF curves and the ARF values, we consider the limiting cases when

u_{res} >> 1 (very fast basin response relative to the rainfall evolution rate) and u_{res} << 1 (very slow basin response) and denote by $u_{ad,x}$ and $u_{ad,y}$ the components of the normalized advection velocity vector in the x and y directions, respectively.

For u_{res} >> 1, the Lagrangian observation parallelogram is highly elongated in the spatial direction and is approximated well by a rectangle with side lengths $L' = L$ and $D' = D\sqrt{1+u_{ad,x}^2}$, as shown in Figure 5a. For u_{res} << 1 the parallelogram is highly elongated in the temporal direction and is approximated well by a rectangle with side lengths $L' = L/\sqrt{1+u_{ad,y}^2}$ and $D' = D\sqrt{1+u_{ad}^2}$; see Figure 5b. In summary, the parameter transformations from a Eulerian to a Lagrangian coordinate system are

$$
\begin{aligned}
u_{res} \gg 1 \quad & \begin{cases} L' = L \\ D' = D\sqrt{1+u_{ad,x}^2} \\ T' = T\sqrt{1+u_{ad,x}^2} \end{cases} \\
u_{res} \ll 1 \quad & \begin{cases} L' = L/\sqrt{1+u_{ad,y}^2} \\ D' = D\sqrt{1+u_{ad}^2} \\ T' = T\sqrt{1+u_{ad}^2} \end{cases}
\end{aligned}
\tag{12}
$$

Notice that, when sampling along a line segment, the effective parameters depend not only on the magnitude but also on the direction of rainfall advection relative to the sampling line.

(c) Averaging Rainfall over a Disc

When sampling over a disc of diameter L, the direction of rainfall advection does not matter; see Figure 4c. In this case the effect of advection is to change L, D and T to L', D', and T' given by

$$u_{res} >> 1 \quad \begin{cases} L' = L \\ D' = D \\ T' = T \end{cases}$$

$$u_{res} << 1 \quad \begin{cases} (L')^2 = L^2/\sqrt{1+u_{ad}^2} \\ D' = D\sqrt{1+u_{ad}^2} \\ T' = T\sqrt{1+u_{ad}^2} \end{cases} \tag{13}$$

Notice that when $u_{res} << 1$ the averaging Lagrangian region is approximated as a cylinder with circular basis of area $a' = a/\sqrt{1+u_{ad}^2}$. Scaling results for IDAF and ARF including advection are obtained by replacing L, D and T on the right hand sides of equations (8)-(11) with the expressions for the effective parameters L', D' and T' in equations (12) and (13). The final results are summarized in Table 1 for very elongated basins (approximated as line segments) and Table 2 for regular basins (approximated as discs).

Tables 1 and 2 show that advection does not change the asymptotic algebraic behaviors of the ARF with D, L, and T. However, advection affects the prefactors of those asymptotic relations. To appreciate the practical importance of this effect, consider typical ranges of the velocity parameters v_{rain} and v_{ad}. As mentioned earlier, v_{rain} varies approximately from 5 to 20 Km/h. The advection velocity v_{ad} usually takes values between 30 and 50 Km/h at small scales (a few kilometers) and between 20 and 40 Km/h at large scales (100 or more kilometers); see for example Martin and Schreiner (1981), Kawamura *et al*. (1996), Deidda (2000) and the review in Langousis (2004). One concludes that u_{ad} varies from 0 to almost 5, and thus the effect of advection may be as large as a factor of 2 on the ARF.

2.4 Numerical Validation

We conclude this section by numerically validating the theoretical results on the ARF, first for $v_{ad} = 0$ and then for $v_{ad} \neq 0$. For the case without advection we use a binary cascade representation of rainfall in two spatial dimensions plus time. The model has lognormal generator B_r and moment-scaling function $K(q) = C_1(q^2 - q)$ with parameter $C_1 = 0.1$. The outer scale of multifractal behavior is fixed to 2^9 cascade cells in each spatial and temporal direction. Hence $d_{max} = l_{max} = 2^9$. Simulation is limited to the parallelepiped with spatial dimensions $2^6 \times 2^6$ and temporal dimension 2^9, and the basin is assumed to be a square with side length at most 2^5 cells. Similarly temporal averaging is over at most 2^5 cells. This means that L and D range from 2^{-9} to 2^{-4}. The $2^6 \times 2^6 \times 2^9$ parallelepiped might represent the rainy season of one year. While this is a highly idealized representation of rainfall, it should suffice for the purpose of validating the theoretical results.

Numerical estimation of the ARF requires calculation of average rainfall intensities at the catchment and rain-gauge scales, the latter assimilated to a point. To obtain these averages, the cascade is generated down to unit space-time cells and then differently "dressed" to produce areal average and point values, as described below.

Denote by $I_b(x, y, t)$ the "bare" rainfall intensity in the unit tile centered at (x, y, t). This is the rainfall intensity obtained at level 9 of the cascade construction procedure. The actual ("dressed") rainfall intensity at that unit scale is obtained as

$$I_{d,3}(x, y, t) = Z_3 \, I_b(x, y, t) \tag{14}$$

where the subscripts b and d stand for bare and dressed, respectively, and Z_3 is the dressing factor for the 3-dimensional cascade.

Consider now a raingauge inside this tile, for example at location (x, y). During the unit time interval centered at t, the average rainfall intensity $I_{d,1}(x, y, t)$ measured by the raingauge is

$$I_{d,1}(x, y, t) = Z_1 \, I_b(x, y, t) \tag{15}$$

Equation (15) is analogous to equation (14), except that Z_1 is the dressing factor of a 1-dimensional cascade with the same cascade generator as the three-dimensional cascade.

For each simulated season, one can numerically estimate the ARF values for different L and D as the ratio between the maximum average rainfall inside the basin and at a point. Figure 6a shows the iso-ARF lines obtained by averaging the rainfall maxima for different L and D over 10 independently simulated seasons. These values have a return period T of about one season (or one year).

In Figure 6a one observes that the iso-lines are essentially straight with a 45-degree slope, as predicted by theory. Also the theoretical scaling relation for large L/D (with exponent $\gamma_1 = 0.532$), is very closely matched by the simulation results; see Figure 6b. An equally good correspondence between simulation and theoretical results has been obtained using more general beta-lognormal cascades, which are able to represent the alternation of rainy and dry space-time regions (Langousis, 2004).

The validation of results with nonzero advection is computationally more demanding because the simulation region must be large enough to include the slanted rainfall observation region in the Lagrangian reference. To reduce the numerical effort, we consider the case when rainfall is observed along a line segment of length L and advection is parallel to that segment. The rainfall model is a 2-dimensional (one space dimension plus one time dimension) binary lognormal cascade and simulation is in a $2^{10} \times 2^{10}$ Lagrangian region. Hence $d_{max} = l_{max} = 2^{10}$. Except for the different size of the simulation region and the lower dimensions (2 rather than 3), the rainfall model is identical to that for no advection.

In analogy with equations (14) and (15), the dressed measures $I_{d,2}(y, t)$ and $I_{d,1}(y, t)$ needed to calculate the ARF are obtained as

$$I_{d,1}(x_, y, t) = Z_1\, I_b(x_, y, t)\ , \qquad I_{d,2}(x_, y, t) = Z_2\, I_b(x_, y, t) \tag{16}$$

Empirical estimates of the ARF have been obtained by averaging extreme rainfalls over 20 independently simulated seasons. Figure 7 compares results for $v_{ad} = 0$ (no advection, lower curve), $v_{ad} = 4$ space units per unit time, and $v_{ad} = 8$ space units per unit time. The theoretical effects of advection can be found from Table 1 for the case $u_{ad,x} = 0$. For $C_1 = 0.1$, one obtains $\gamma_1 = 2\sqrt{C_1} - C_1 = 0.532$ and $q_1 = 1/\sqrt{C_1} = 3.162$. Moreover, for $u_{res} >> 1$, T finite and $L \rightarrow 0$, Table 1 gives the advection correction factor $(1+u_{ad}^2)^{0.108}$. Hence the curves for $u_{ad} = 4$ and the $u_{ad} = 8$ in Figure 7 should be shifted upwards by 0.44 and 0.65, respectively, relative to the $u_{ad} = 0$ case. The numerical results agree very well with these theoretical predictions.

3. Deviations from Multifractality

Stationary multifractal fields result from cascade constructions in which non-negative fluctuations $Y_j(x, y, t)$ at different scales $s_j = s_0\, r^{-j}$ are multiplied. Here $s_0 > 0$ and $r > 1$ are constants and $j = 1, 2, \ldots$ is the cascade level. A necessary condition for scale invariance is that the fluctuations $Y_j(x, y, t)$ be statistically identical to $Y(r^j x, r^j y, r^j t)$, where $Y(x, y, t)$ is some non-negative mean-1 stationary process called the generator of the cascade.

Several studies have found that rainfall may indeed be represented by a multiplicative cascade, but the amplitude of the fluctuation Y_j decreases as the cascade level j increases; see for example Perica and Foufoula-Georgiou (1996), Menabde *et al*. (1997), Menabde and Sivapalan (2000), and Veneziano *et al*. (2004).

Models that in different ways capture this feature include the wavelet representation of Perica and Foufoula-Georgiou (1996), the bounded cascades of Menabde *et al*. (1997) and Menabde and Sivapalan (2000), and the universal multifractal processes of Schertzer and Lovejoy (1987), the latter when the fractional integration parameter H is nonzero. Here we use a bounded cascade model to assess how departure from multifractality affects the ARF.

The construction of a bounded cascade is identical to that of a multifractal cascade, except that the standard deviation of the generator σ_y (or some other dispersion measure like the C_1 coefficient) decreases as the cascade level j increases. To illustrate the effect on the ARF, we assume that rainfall is a lognormal bounded cascade in space and time, with multiplicity 2 in all three coordinate directions and a generator B_j that varies with the cascade level j as

$$\ln(B_j) \sim N\left(-\frac{\sigma^2(j)}{2}, \sigma^2(j)\right) \tag{17}$$

where $N(\mu, \sigma^2)$ is the normal distribution with mean value μ and variance σ^2. The standard deviation $\sigma(j)$ decays linearly with j as shown in Figure 8a. This is similar to the decay found by Menabde and Sivapalan (2000) and Perica and Foufoula-Georgiou (1996); see Langousis (2004). Except for this change, the numerical simulation procedure is the same as in Section 2.4.

Figure 8b shows how the ARF varies with L and D. This figure should be compared with Figure 6a, which displays similar results under multifractality. Notice that $\sigma_B(0) = 0.385$ corresponds to $C_1 = 0.1$; hence the two cascade models have the same variability at the largest scale; see Figure 8a. Relative to Figure 6a, the contour lines in Figure 8b are displaced upwards because the bounded-cascade process is smoother than the multifractal process. Therefore, for small L, spatially averaged rainfalls in the bounded cascade are nearly identical to point rainfalls. A second important effect is that the contour lines in Figure 8b are not straight, reflecting lack of scale invariance of the bounded cascade. In particular, for large L and small D the lines are very flat (since further reducing D does not affect much the rainfall averages) and their slope increases towards 1 as L decreases or D increases.

4. The Effect of Sparse Spatial Sampling

When the ARF is estimated from raingauge measurements, as is typically done in practice, the rainfall intensity in a region is estimated as the average (or weighted average) of raingauge measurements at points inside the region. Unless the raingauge spacing varies proportionally to the size L of the region, this operation destroys any scaling property the ARFs might have.

Sparse point sampling can be easily simulated. Suppose that the resolution of the cascade simulation is such that at most one raingauge site falls inside each cascade tile. Then the only difference with the procedure described in Section 2.4 is that one must multiply the "bare" rainfall intensity in the cascade tile that hosts a raingauge by the 1-dimensional random dressing factor Z_1 instead of the three-dimensional factor Z_3.

To illustrate the effect of sparse spatial sampling, we use again the 3-dimensional lognormal cascade model of Figure 6a. Figure 9 shows ARF results when the raingauge stations are arranged on a regular square grid with a density of 1 station per four cascade tiles. Comparison with Figure 6a shows that for large L the ARF values are not influenced by sparse sampling. However, significant differences are evident for small L. In the limiting case when L equals the inter-station distance (this happens here for $\log_2(L) = 1$), the spatially averaged rainfall is estimated as the rainfall at the only station inside the region. This is why the ARF in Figure 9 is identically 1 along the lower boundary. The contour lines of the ARF, which have a 45-degree slope for large L, must necessarily bend to remain above this horizontal ARF = 1 line. It is emphasized that in this case the curvature of the ARF contour lines is due to lack of scaling of the observation grid not lack of scaling of the rainfall field. Hence the differences between Figures 6a and 9 reflect bias due to sparse sampling.

5. Interpretation of Empirical Areal Reduction Factors

To conclude, we examine features of empirical ARFs in the light of previous model-based results. For this purpose, we use the ARF data of the Natural Environmental Research Council (NERC, 1975). The data comprise ARF estimates from thirteen basins in the United Kingdom, with areas ranging from 10 to 18 000 Km^2 and durations from 2 minutes to 25 days; see Table 3. According to NERC, these ARFs refer to rainfall events with return periods of 2-3 years.

NERC (1975) interpolated and extrapolated the original ARF values to produce charts that cover a wider range of catchment areas (from 1 to 30 000 Km^2) and averaging durations (from 1 minute to 25 days). The interpolated values fit well the original data for some but not all combinations of a and d. To more faithfully reflect the original data, we have re-interpolated the original values in Table 3 using 1st order triangulation. The results are shown in Figure 10.

One may distinguish four regions in Figure 10 where the ARF contour lines have different behaviors. Region 1 displays simple scaling of the ARF with a and d. Specifically, the ARF is constant for $d \propto \sqrt{a}$ (for $d \propto l$, considering that basin shape is essentially independent of basin size). This agrees with results obtained in Sections 2.1 and 2.2 under the assumption that rainfall is multifractal in space and time.

In Region 2, the contour lines become flatter as a or d decreases. This is also what happens if, at small space-time scales, rainfall behaves like a bounded cascade; see Section 3. In Region 3, the contour lines have higher curvature and become nearly parallel to the d-axis for small a and d. Sparse spatial sampling produces a similar effect, as l approaches the inter-station distance; see Section 4. Finally, in Region 4 where $d/\sqrt{a}$ is large, the contour lines are more widely spaced than under exact multifractality. Langousis (2004) has shown that this feature could be due to high lacunarity of the rain support at synoptic and meso-scales. However this is only a tentative conclusion, since the behavior of the ARF in Region 4 is poorly constrained by the data.

Next we show how the results in Figure 10 can be quantitatively reproduced. To reduce the computational effort, we focus on the region with a in the range 30-1 000 Km^2 and d in the range 15 min-6 hours. This includes the various sub-regions mentioned above except Region 1, where the ARF behaves consistently with multifractal cascades and need no further confirmation.

For Regions 2 and 3, we use a bounded Log-Normal (LN) cascade representation of rainfall in two spatial dimensions plus time. The cascade has multiplicity 2 in all directions. The cascade generator B_j satisfies equation (17), where $\sigma(j)^2$ varies with the cascade level j according to Figure 11a. Figure 11a approximates the empirical findings of Menabde and Sivapalan (2000) for temporal rainfall. For durations longer than those in Menabde and Sivapalan (2000), we assume that the distribution of the generator is the same as that at the largest scale available.

The numerical simulation procedure is the same as in Sections 2 and 3, with tiles at the highest resolution representing space-time regions of area 1Km^2 and duration ¼ hours. To model sparse spatial sampling, we calculate area intensities as averages at geographical points with regular spacing and a density of 1 raingauge per 4 Km^2. This is comparable to the average density in the NERC data; see NERC (1975), Vol. IV, p. 24.

Figure 11b shows ARF results averaged over 10 independently simulated seasons. The contour lines in Regions 2 and 3 are in good agreement with Figure 10. Notice in particular the high curvature in Region 3, which is caused primarily by sparse sampling. In Region 4, the agreement is not as good. As noted above, better agreement in this region can be achieved through the inclusion of large-scale lacunarity (Langousis, 2004). However, in Region 4 the ARF is close to 1. Hence its accurate determination is not critical in practice and the simple bounded lognormal model illustrated in Figure 11 should suffice.

6. Conclusions

We have analyzed the scaling properties of the areal reduction factor (ARF) under the condition that space-time rainfall has exact or approximate multifractal scale invariance. We have considered regular and highly elongated basins, quantified the effect of rainfall advection, and investigated the bias when estimating the ARF from sparse raingauge networks.

We have found that under perfect multifractality the ARF has asymptotic scaling behaviors with L/D and T, where L is the largest linear size of the region of rainfall averaging, D is the duration of averaging, and T is the return period. Specifically, ARF ~ $(L/D)^{-\alpha} T^{\beta}$ for $(L/D) \to \infty$, $(L/D) \to 0$, or $T \to \infty$. The non-negative constants α and β depend somewhat on the geometry of the region (regular or highly elongated) and differ in the three limiting cases above, but are independent of rainfall advection and can be found easily from the multifractal properties of rainfall. The behavior for $(L/D) \to 0$ is simply ARF $\to 1$, whereas the other two limiting cases are non-trivial.

The ARF depends on T in two ways: through the term T^{β} and through α, which has different values for T finite and $T \to \infty$. The latter is usually the dominant influence. The effect of T on the ARF may be numerically important. This confirms qualitatively the findings of Bell (1976), Asquith and Famiglietti (2000) and De Michele *et al.* (2001). A reason why empirical studies like NERC (1975) failed to detect significant T dependence is that available space-time rainfall records allow ARF estimation over only a small range of return periods.

For $(L/D) \to \infty$ or $T \to \infty$, the above scaling relationships have prefactors that depend on the rainfall advection velocity parameter u_{ad} and to a lesser extent the shape of the basin. For nonextremely elongated basins this prefactor is of the type $(1+u_{ad}^2)^c$, where c is a positive constant with typical values between 0.1 and 0.5. Hence, depending on u_{ad} (see Section 2.3), the effect of advection on the ARF may be as large as 2. To our knowledge, this is the first time that this effect has been quantified. Of course, advection is implicitly included in empirical estimates of the ARF, but its effect should be added when the ARF is theoretically estimated from non-advecting rainfall models.

We have studied the effect of basin shape by considering two limiting cases: basins with nearly circular or square shape and highly elongated basins that can be approximated as line segments. Basin shape affects the exponent β when $T \rightarrow \infty$ and the prefactor in the case of advecting rainfall. These effects are generally small (that on β is important for T beyond the typical range of return periods encountered in practice). Also, very highly elongated basins are rare. Hence, for most applications, one may use the results for regularly shaped regions.

Rainfall has been observed to deviate from perfect multifractality. The main deviation is that local intensity fluctuations are smaller than required for scale invariance. We have modeled this behavior by using "bounded cascades", in which the fluctuations at smaller scales are progressively reduced in amplitude. As a result of this reduction, the ARF is closer to 1 and the scaling properties mentioned above are lost. In particular, the ARF no longer depends on L and D through the ratio L/D and its contour lines on the $(\log(L), \log(D))$-plane are no longer straight, becoming flatter as L and D decrease. A curvature of this type is often noted in empirical ARF charts.

Another reason for the curvature of empirical contour lines is the bias induced by estimating area rainfalls from point (raingauge) data. As L approaches the inter-station distance, only one station is used to estimate area rainfall and the ARF is consequently calculated as 1. This saturation causes the ARF contours to bend in a way similar to the case of bounded cascades. We have found that both deviations from multifractality and sparse sampling bias affect NERC's (1975) empirical ARF charts.

Although this study covers a wide range of factors affecting the ARF, some issues remain unexplored. One is the existence and effect of anisotropic scaling of rainfall in space and time (see for example Venugopal et al., 1999). Qualitatively, anisotropic scaling changes the 45^{o} slope of the contour lines on the (log(L), log(D))-plane. No such tilt was observed in NERC's (1975) ARF results. However, the absence of scaling anisotropy (and other aspects of rainfall and ARF modeling discussed in the paper) should be confirmed through additional rainfall data analysis.

Sparseness of the NERC (1975) data set did not allow us to adequately investigate the ARF behavior for large D/L ratios. While also this issue could be resolved by using more extensive data sets, the fact that for large D/L the ARF is close to 1 makes its resolution less critical for practical applications.

Acknowledgments

This work was supported in part by the Department of Civil and Environmental Engineering of MIT under the *Schoettler Fellowship*, in part by the National Science Foundation under Grant No. EAR-0228835, and in part by the *Alexander S. Onassis* Public Benefit Foundation under Scholarship No. F-ZA 054/2004-2005.

References

Asquith, W.H. and Famiglietti, J.S. (2000) Precipitation areal-reduction factor estimation using an annual-maxima centered approach, *J. Hydrol.*, **230**, 55-69.

Austin, P.M. and House, R.A. (1972) Analysis of the structure of precipitation patterns in New England *J. Appl. Meteor.*, **11**, 926-935.

Bacchi B. and Ranzi R. (1996) On the derivation of the areal reduction factor of storms, *Atm. Res.*, **42**, 123-135.

Bell, F.C. (1976) The areal reduction factors in rainfall frequency estimation, Rep. No. 35, Institute of Hydrology, Wallingford.

Castro, J., Cârsteanu, A., and Flores, C. (2004) Intensity – duration – area – frequency functions for precipitation in a multifractal framework, *Physica A*, **338**, 206-210.

Deidda, R. (2000) Rainfall down scaling in a space-time multifractal framework, *Wat. Resour. Res.*, **36**(7), 1779-1794.

De Michele , C., Kottegoda, N.T., and Rosso, R. (2001) The derivation of areal reduction factor of storm rainfall from its scaling properties, *Wat. Resour. Res.*, **37**(12), 3247-3252.

Fraedrich, K. and Larnder, C. (1993) Scaling Regimes of Composite Rainfall Time Series, *Tellus*, **45A**, 289-298.

Gupta, V.K. and Waymire, E. (1990) Multiscaling properties of spatial rainfall and river flow distributions, *J. Geophys. Res.,* **95**, 1999-2009.

Gupta, V.K. and Waymire, E. (1993) A statistical analysis of mesoscale rainfall as a random cascade, *J. Appl. Meteorol.*, **32**(2), 251-267.

Hershfield, D.M. (1962) Extreme rainfall relationships. Proc. Am. Soc. Civ. Eng., *J. Hydraul. Div.*, HY**6**(11), 73-79.

Hubert, P., Bendjoudi, H., Schertzer, D., and Lovejoy, S. (1998) A Multifractal explanation for rainfall intensity-duration-frequency curves, Int. Proc. of "*Heavy rains and flash floods*" , Instanbul, Turkey, 21-28.

Kawamura, A., Jinno, K., Berndtsson, R., and Furukawa, T. (1996) Parameterization of rain cell properties using an advection-diffusion model and rain gage data. *Atm. Res.*, **42**, 67-73.

Koutsoyiannis, D. (1997) *Statistical Hydrology* (in Greek), 4th Ed., Dpt. of Water Resources, Hydraulic and Maritime Engineering - National Technical University of Athens, Greece.

Langousis, A. (2004) *The Areal Reduction Factor a Multifractal Analysis*, MSc Thesis, 117 pages, Department of Civil and Environmental Engineering, MIT, Cambridge, Mass.

Leclerc, G. and Schaake, J.C. (1972) *Derivation of Hydrologic Frequency Curves*. Report 142, Dept. of Civil Engineering, MIT, Cambridge, Mass., 151 pp.

Lovejoy, S. and Schertzer D. (1995) Multifractals and rain, *New Uncertainty Concepts in Hydrology and Hydrological Modeling*, Ed. A. W. Kundzewicz, 62-103, Cambridge Press.

Martin, D.W. and Schreiner, A.J. (1981) Characteristics of West African and East Antlantic Cloud Clusters: A Survey from GATE. *Monthly Weather Review*, **109**, 1671-1688.

Menabde, M., Harris, D., Seed, A., Austin, G. and Stow, D. (1997) Multiscaling properties of rainfall and bounded random cascades, *Wat. Resour. Res.*, **33**(12), 2823-2830.

Menabde, M. and Sivapalan, M. (2000) Modelling of rainfall time series and extremes using bounded random cascades and Levy-stable distributions, *Wat. Resour. Res.*, **36**(11), 3293-3300.

Natural Environmental Research Council (NERC) (1975), *Flood Studies report*, Institute of Hydrology, Wallingford, U.K.

Olsson, J. (1995) Limits and Characteristics of the Multifractal Behavior of a High-Resolution Rainfall Time Series, *Nonlinear processes in Geophysics*, **2**, 23-29.

Olsson, J., Niemczynowicz, J. and Berndtsson, R. (1993) Fractal Analysis of High-Resolution Rainfall Time Series, *J. Geophys. Res.*, **98**(D12), 23 265-23 274.

Omolayo, A.S. (1993) On the transposition of areal reduction factors for rainfall frequency estimation, *J. Hydrol.*, **145**, 191-205.

Orlanski, I. (1975) A Rational Subdivision of Scales for Atmospheric Processes. *American Meteorological Society,* **56**(5), 527-530.

Perica, S. and Foufoula-Georgiou, E. (1996) Model for multiscale disaggregation of spatial rainfall based on coupling meteorological and scaling descriptions, *J. Geophys. Res.* **101**(D21), 26 347-26 361.

Roche, M. (1966) *Hydrologie de Surface*, Gauthier-Villars, Paris, France.

Rodriguez-Iturbe, I. & Mejia, J.M. (1974) On the transformation of point rainfall to areal rainfall, *Water Resour. Res.*, **10**(4), 729-735.

Schertzer, D. and Lovejoy, S. (1987) Physical modeling and analysis of rain and clouds by anisotropic scaling of multiplicative processes, *J. Geophys. Res.*, **92**, 9693-9714.

Singh, V. P. (1992) *Elementary Hydrology* , Prentice-Hall, New Jersey, U.S.A.

Sivapalan, M., Blöschl G. (1998) Transformation of point rainfall: Intensity-duration-frequency curves, *J. Hydrol.*, **204**, 150-167.

Veneziano, D. (1999) Basic properties and characterization of stochastically self-similar processes in R^D, *Fractals,* **7**(1), 59-78.

Veneziano, D. and Furcolo, P. (2002a) Multifractality of rainfall and intensity-duration-frequency curves, *Wat. Resour. Res.*, **38**(12), 1306-1317.

Veneziano, D. and Furcolo, P. (2002b) Scaling of multifractal measures under affine transformations, *Fractals*, **10**(2), 147-156.

Veneziano, D., Furcolo, P. and Iacobellis, V. (2005) Imperfect Scaling of Time and Space-Time Rainfall, *J. Hydrol*. (in press).

Venugopal, V., Foufoula-Georgiou, E. and Sapozhnikov, V. (1999), Evidence of Dynamic Scaling in Space-Time Rainfall, *J. Geophys. Res.*, **104**(D24): 31 599-31 610.

Viessman, W., and Lewis, G. (2003) *Introduction to Hydrology*, Pearson Education Inc., Upper Saddle River, NJ.

Willems, P. (2000), Compound intensity/duration/frequency-relationships of extreme precipitation for two seasons and two storm types, *J. Hydrol.* **233**: 189-205.

Figure Captions

Figure 1: Moment scaling function $K(q)$ and parameters γ_1, q_1 and q_n*.

Figure 2: Multifractal scaling of rainfall in space and time.

Figure 3: Illustration of multiple ranges of algebraic tail behavior for $I(t|L_1,L_2,D)$.

Figure 4: The effect of advection for sampling at a point, along a line segment and inside a disc, over duration D.

Figure 5: Observation of rainfall along a line segment (see Figure 4b). Approximation of the averaging regions in a Lagrangian reference.

Figure 6: (*a*) ARF scaling behavior with L and D, and the associated fast- (i.e. $L/D > 5$) and slow-response (i.e. $L/D < 5$) regions. Rainfall is a lognormal multifractal process in space and time with coefficient C_1=0.1 and associated γ_1 = 0.532. (*b*) Cross-section along -45^o lines, showing dependence of the ARF on L/D.

Figure 7: ARF dependence on L/D for different advection velocities. The indicated slope γ_1 and shifts are theoretical values.

Figure 8: (*a*) Standard deviation of the generator B_j of a bounded cascade model of rainfall. (*b*) Contour plot of the ARF for the bounded cascade model in (*a*) and $T = 1$.

Figure 9: Contour plot of the ARF in the case of sparse sampling. The rainfall model is the same as in Figure 6a. Raingauge stations are arranged on a square grid with a density of 1 station per four cascade tiles.

Figure 10: Interpolation of ARF values in Table 3. The square region corresponds to the ranges of area and duration in Figure 11.

Figure 11: (*a*) Standard deviation of the bounded cascade generator used to produce the ARF values in (*b*). Rainfall is measured at points on a square grid with density of 1 raingauge per 4 Km^2.

	Very slow response region $u_{res} << 1$	**Very fast response region $u_{res} >> 1$**
Scaling	$I(t\mid L, D) \approx_d B_{r_D} I(r_D t\mid r_L L, r_D D)$, $r_L, r_D \geq 1$ (no dependence on L)	$I(t\mid L, D) \approx_d B_{r_L} I(r_L t\mid r_L L, r_D D)$, $r_L, r_D \geq 1$ (no dependence on D)
Extremes	$i(L, D, T, u_{ad}) \propto$ $\begin{cases} (1+u_{ad}^2)^{\frac{1}{2}\left(\frac{1}{q_1}-\gamma_1\right)} D^{-\gamma_1} T^{\frac{1}{q_1}}, \text{ for } \begin{cases} D\to 0 \\ T \text{ finite} \end{cases} \\ (1+u_{ad}^2)^{\frac{1}{2}\left(\frac{1}{q_n^*}-1\right)} D^{-1} T^{\frac{1}{q_n^*}}, \text{ for } \begin{cases} D \text{ finite} \\ T\to\infty \end{cases} \end{cases}$ (no dependence on L)	$i(L, D, T, u_{ad}) \propto$ $\begin{cases} (1+u_{ad,x}^2)^{\frac{1}{2q_1}} L^{-\gamma_1} T^{\frac{1}{q_1}}, \text{ for } \begin{cases} L\to 0 \\ T \text{ finite} \end{cases} \\ (1+u_{ad,x}^2)^{\frac{1}{2q_n^*}} L^{-1} T^{\frac{1}{q_n^*}}, \text{ for } \begin{cases} L \text{ finite} \\ T\to\infty \end{cases} \end{cases}$ (no dependence on D)
$\eta(L, D, T, u_{ad})$	$\eta(L, D, T, u_{ad}) \propto$ $\begin{cases} 1, \text{ for } \begin{cases} D\to 0 \\ T \text{ finite} \end{cases} \\ \left((1+u_{ad}^2)^{½} T\right)^{\left(\frac{1}{q_n^*}-\frac{1}{q_1^*}\right)}, \text{ for } \begin{cases} D \text{ finite} \\ T\to\infty \end{cases} \end{cases}$	$\eta(L, D, T, u_{ad}) \propto$ $\begin{cases} \left(\frac{1+u_{ad,x}^2}{(1+u_{ad}^2)^{1-\gamma_1 q_1}}\right)^{\frac{1}{2q_1}} \left(\frac{L}{D}\right)^{-\gamma_1}, \text{ for } \begin{cases} L\to 0 \\ T \text{ finite} \end{cases} \\ \left(\frac{(1+u_{ad,x}^2)^{\frac{1}{q_n^*}}}{(1+u_{ad}^2)^{\left(\frac{1}{q_1^*}-1\right)}}\right)^{½} \left(\frac{L}{D}\right)^{-1} T^{\left(\frac{1}{q_n^*}-\frac{1}{q_1^*}\right)}, \text{ for } \begin{cases} L \text{ finite} \\ T\to\infty \end{cases} \end{cases}$

Table 1: Scaling of the IDAF curves and the ARFs for very elongated basins of dimensionless length L. The effect of advection is included through the parameter $u_{ad} \neq 0$).

	Very slow response region $u_{res} << 1$	**Very fast response region $u_{res} >> 1$**
Scaling	$I(t \mid L, D) \overset{d}{\approx} B_{r_D} I(r_D t \mid r_L L, r_D D)$, $r_L, r_D \geq 1$ (no dependence on L)	$I(t \mid L, D) \overset{d}{\approx} B_{r_L} I(r_L t \mid r_L L, r_D D)$, $r_L, r_D \geq 1$ (no dependence on D)
Extremes	$i(L, D, T, u_{ad}) \propto$ $\begin{cases} (1+u_{ad}^2)^{\frac{1}{2}\left(\frac{1}{q_1}-\gamma_1\right)} D^{-\gamma_1} T^{\frac{1}{q_1}}, \text{ for } \begin{cases} D \to 0 \\ T \text{ finite} \end{cases} \\ (1+u_{ad}^2)^{\frac{1}{2}\left(\frac{1}{q_3^*}-1\right)} D^{-1} T^{\frac{1}{q_3^*}}, \text{ for } \begin{cases} D \text{ finite} \\ T \to \infty \end{cases} \end{cases}$ (no dependence on L)	$i(L, D, T, u_{ad}) \propto$ $\begin{cases} L^{-\gamma_1} T^{\frac{1}{q_1}}, \text{ for } \begin{cases} L \to 0 \\ T \text{ finite} \end{cases} \\ L^{-1} T^{\frac{1}{q_3^*}}, \text{ for } \begin{cases} L \text{ finite} \\ T \to \infty \end{cases} \end{cases}$ (no dependence on D)
ARF(L, D, T, u_{ad})	$\eta(L, D, T, u_{ad}) \propto$ $\begin{cases} 1, \text{ for } \begin{cases} D \to 0 \\ T \text{ finite} \end{cases} \\ \left((1+u_{ad}^2)^{\frac{1}{2}} T\right)^{\left(\frac{1}{q_3^*}-\frac{1}{q_1^*}\right)}, \text{ for } \begin{cases} D \text{ finite} \\ T \to \infty \end{cases} \end{cases}$	$\eta(L, D, T, u_{ad}) \propto$ $\begin{cases} (1+u_{ad}^2)^{\frac{1}{2}\left(\gamma_1-\frac{1}{q_1}\right)} \left(\frac{L}{D}\right)^{-\gamma_1}, \text{for } \begin{cases} L \to 0 \\ T \text{ finite} \end{cases} \\ (1+u_{ad}^2)^{\frac{1}{2}\left(1-\frac{1}{q_1^*}\right)} \left(\frac{L}{D}\right)^{-1} T^{\left(\frac{1}{q_3^*}-\frac{1}{q_1^*}\right)}, \text{for } \begin{cases} L \text{ finite} \\ T \to \infty \end{cases} \end{cases}$

Table 2: Scaling of the IDAF curves and the ARFs for regularly shaped basins, assimilated to discs of dimensionless diameter L. The effect of advection is included through the parameter u_{ad}.

	Area (sq. km)							
Duration	10	100	1000	1500	5000	8000	10000	18000
2 min	0.67	-	-	-	-	-	-	-
4 min	0.74	-	-	-	-	-	-	-
10 min	0.85	-	-	-	-	-	-	-
15 min	-	0.62	0.39	-	-	-	-	-
30 min	0.88	0.73	0.51	-	-	-	-	-
60 min	0.9	0.77	0.62	-	-	0.47	-	0.4
2 hours	-	0.84	0.75	-	-	0.57	-	0.51
3 hours	-	-	-	-	-	0.64	-	0.57
6 hours	-	-	-	-	-	0.74	-	0.67
1 day	-	0.94	-	0.89	0.84	0.83	0.82	0.81
2 days	-	0.97	-	0.91	0.85	0.85	0.83	0.83
4 days	-	0.97	-	0.92	0.88	0.87	0.87	0.84
8 days	-	0.97	-	0.93	0.89	0.91	0.89	0.87
25 days	-	0.99	-	0.97	0.94	0.95	0.94	0.93

Table 3: ARF values used in NERC (1975).

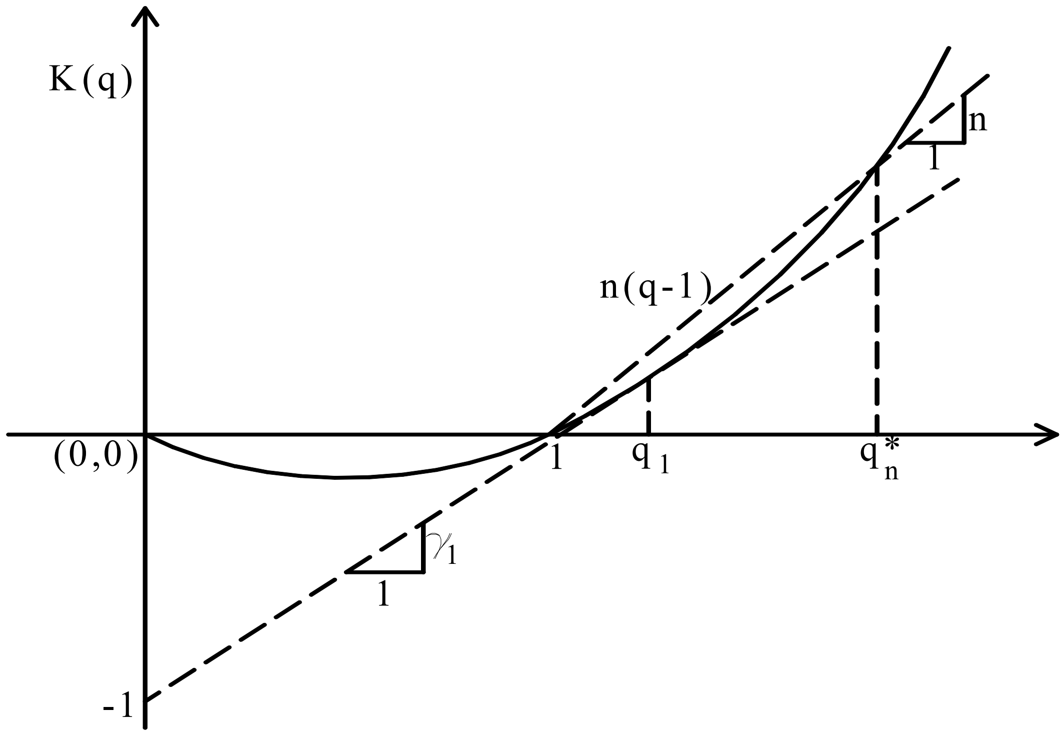

Figure 1: Moment scaling function $K(q)$ and parameters γ_1, q_1 and q_n*.

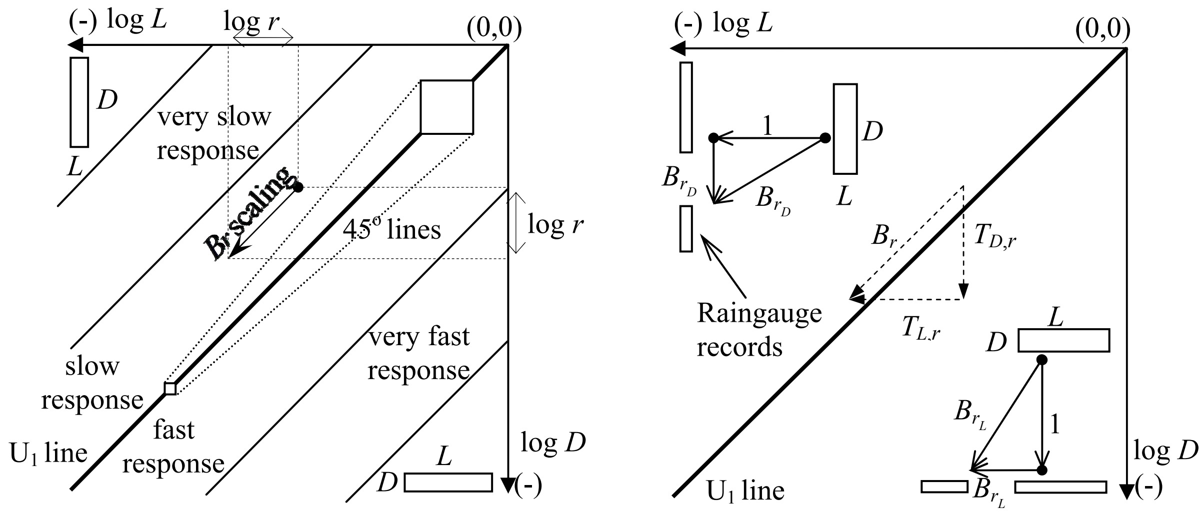

(a) 45° scaling in the [ln(L), ln(D)] plane (b) Schematic representation of scaling relations

Figure 2: Multifractal scaling of rainfall in space and time.

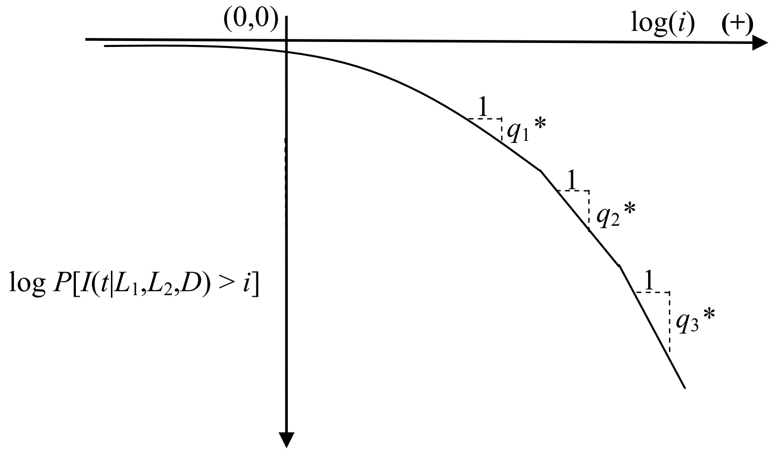

Figure 3: Illustration of multiple ranges of algebraic tail behavior for $I(t|L_1,L_2,D)$.

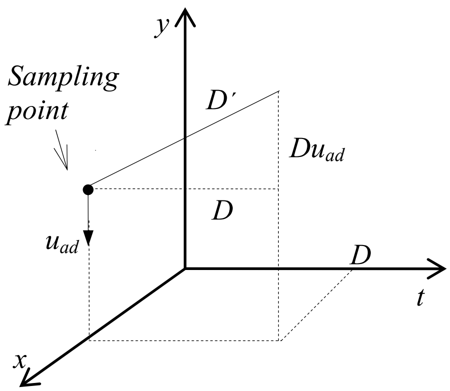

(a) Sampling at a point

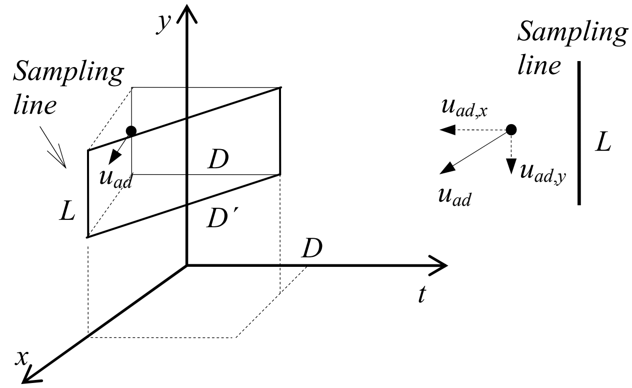

(b) Sampling along a line segment of length L

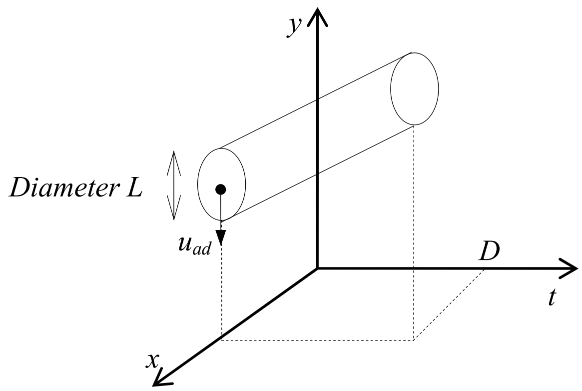

(c) Sampling inside a disc of diameter L

Figure 4: The effect of advection for sampling at a point, along a line segment and inside a disc, over duration D.

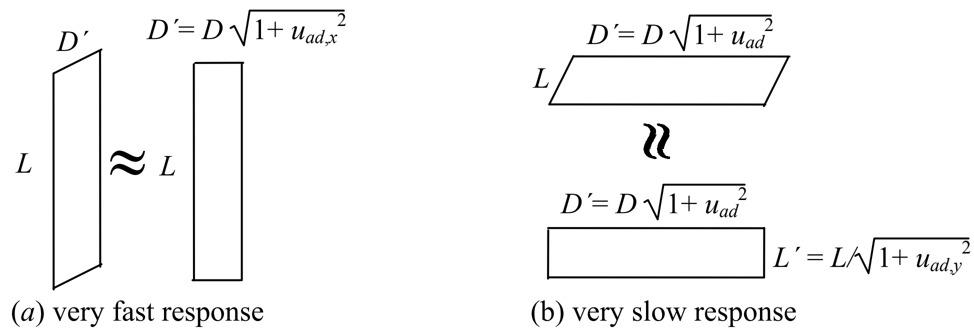

Figure 5: Observation of rainfall along a line segment (see Figure 4b). Approximation of the averaging regions in a Lagrangian reference.

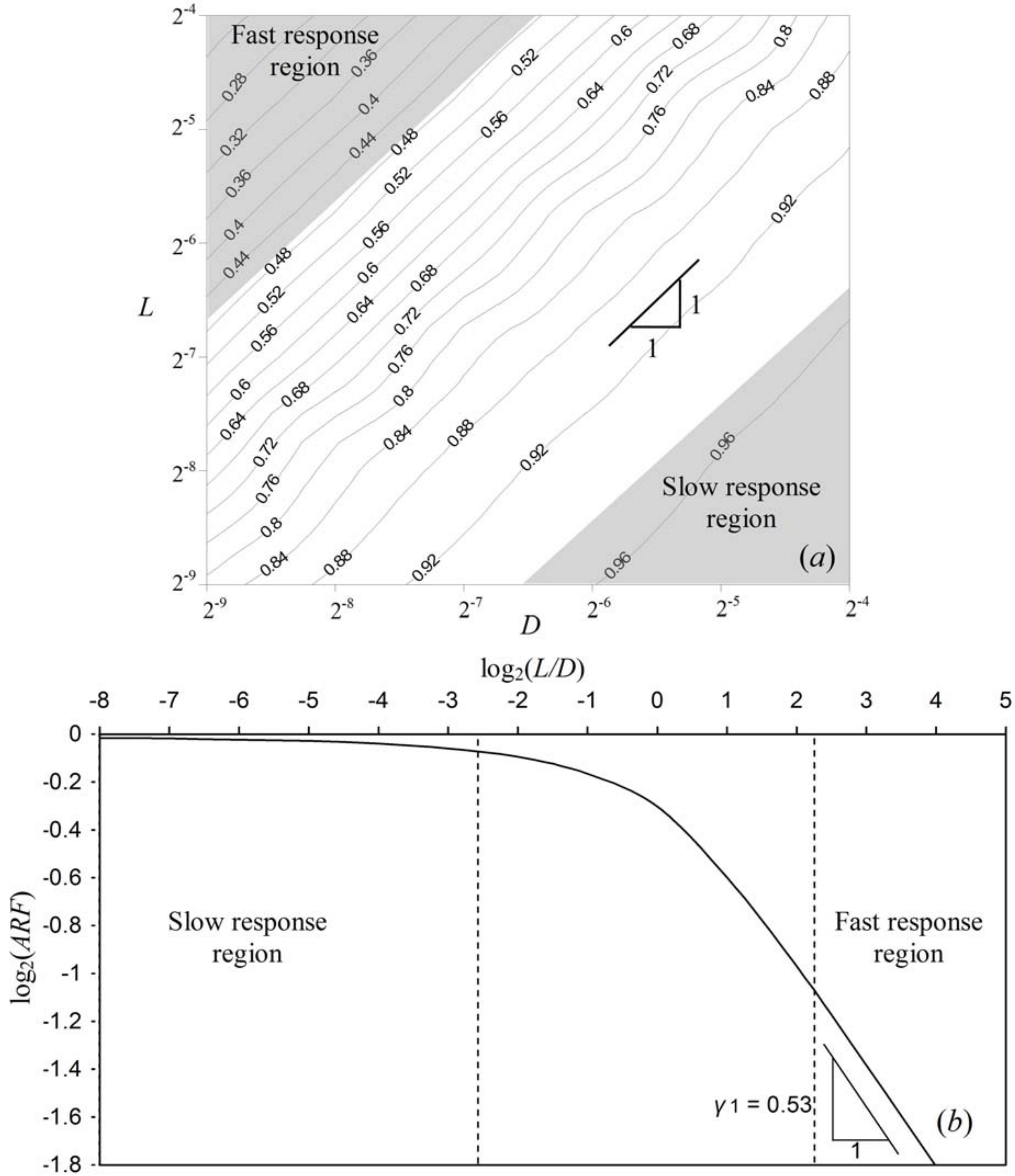

Figure 6: (*a*) ARF scaling behavior with L and D, and the associated fast- (i.e. $L/D > 5$) and slow-response (i.e. $L/D < 5$) regions. Rainfall is a lognormal multifractal process in space and time with coefficient C_1=0.1 and associated γ_1 = 0.532. (*b*) Cross-section along -45° lines, showing dependence of the ARF on L/D.

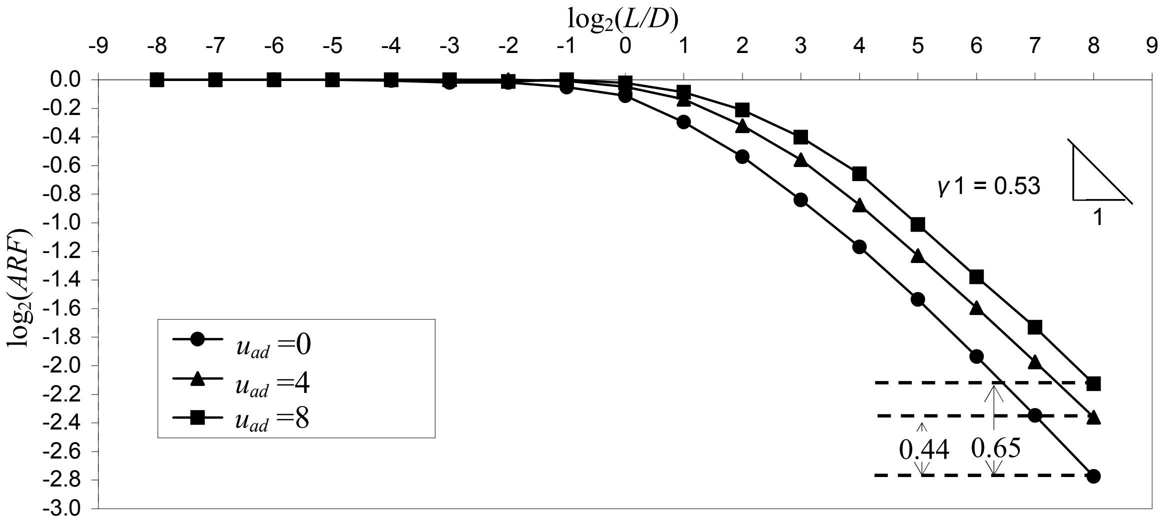

Figure 7: ARF dependence on L/D for different advection velocities. The indicated slope γ_1 and shifts are theoretical values.

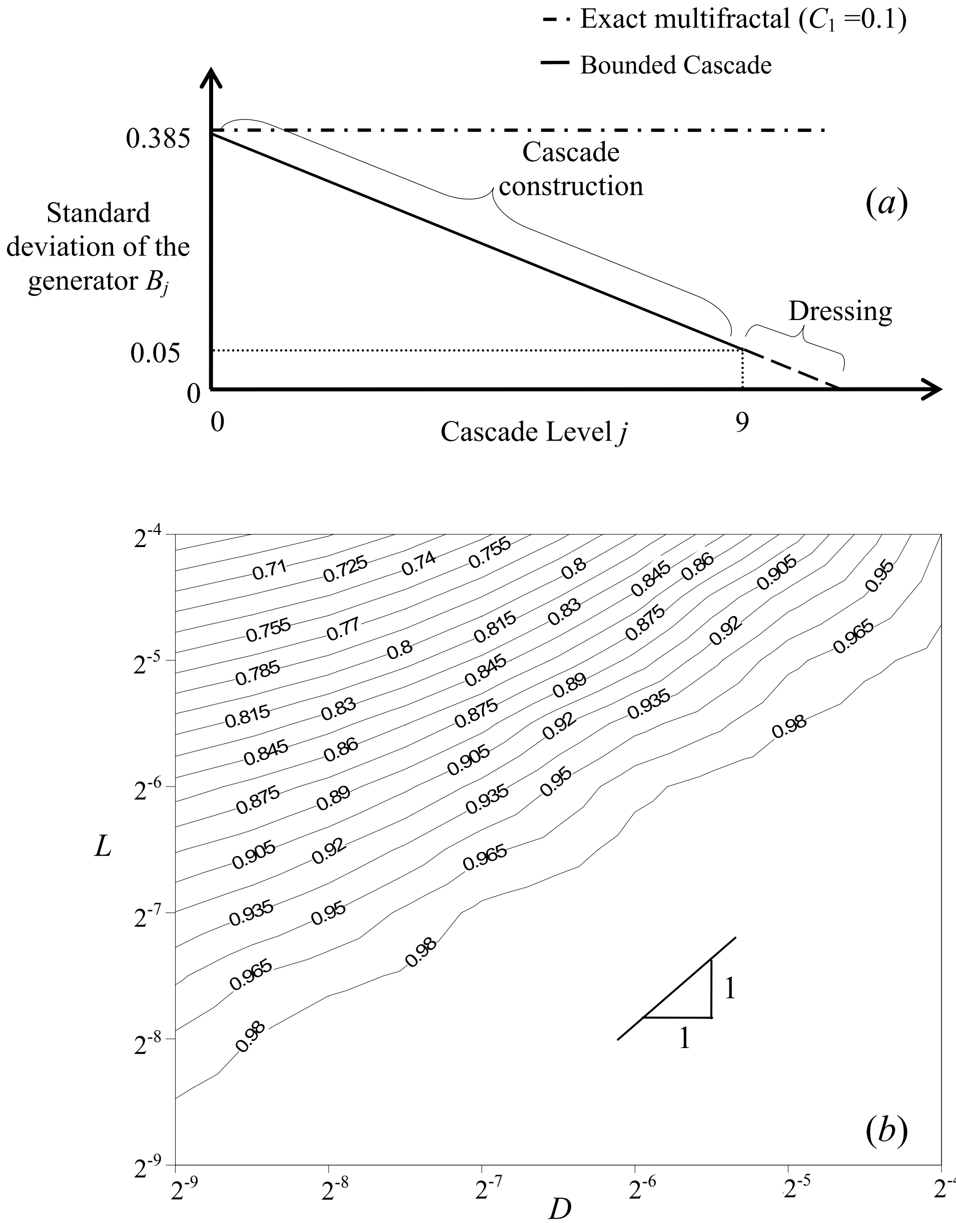

Figure 8: (*a*) Standard deviation of the generator B_j of a bounded cascade model of rainfall. (*b*) Contour plot of the ARF for the bounded cascade model in (*a*) and $T = 1$.

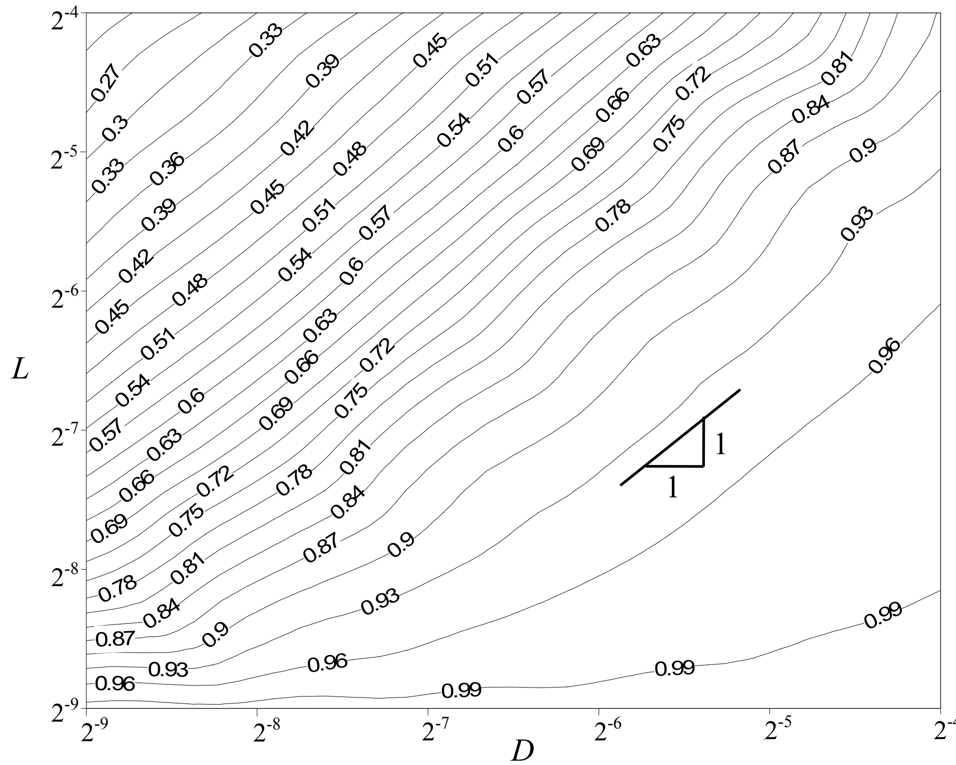

Figure 9: Contour plot of the ARF in the case of sparse sampling. The rainfall model is the same as in Figure 6a. Raingauge stations are arranged on a square grid with a density of 1 station per four cascade tiles.

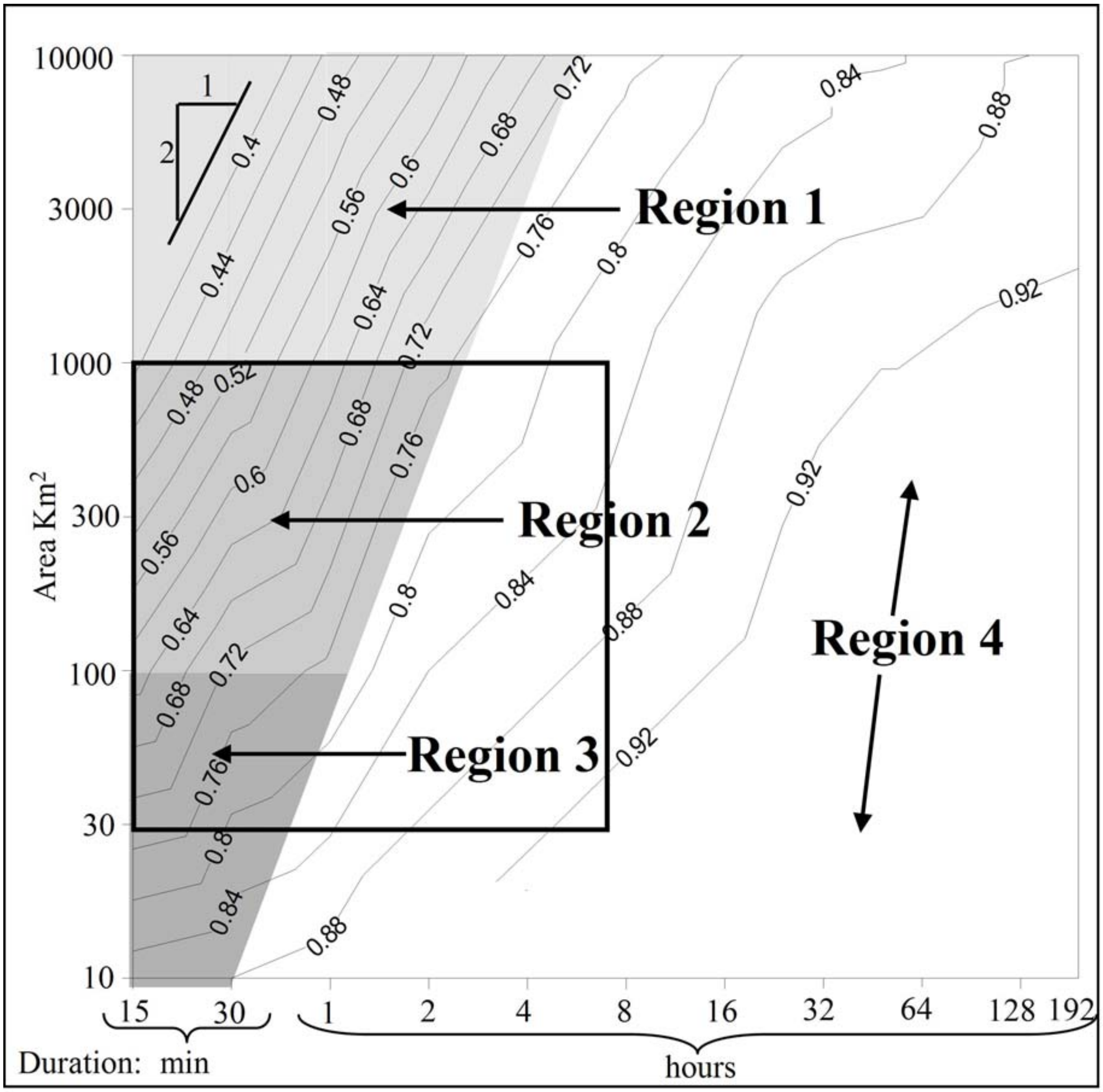

Figure 10: Interpolation of ARF values in Table 3. The square region corresponds to the ranges of area and duration in Figure 11.

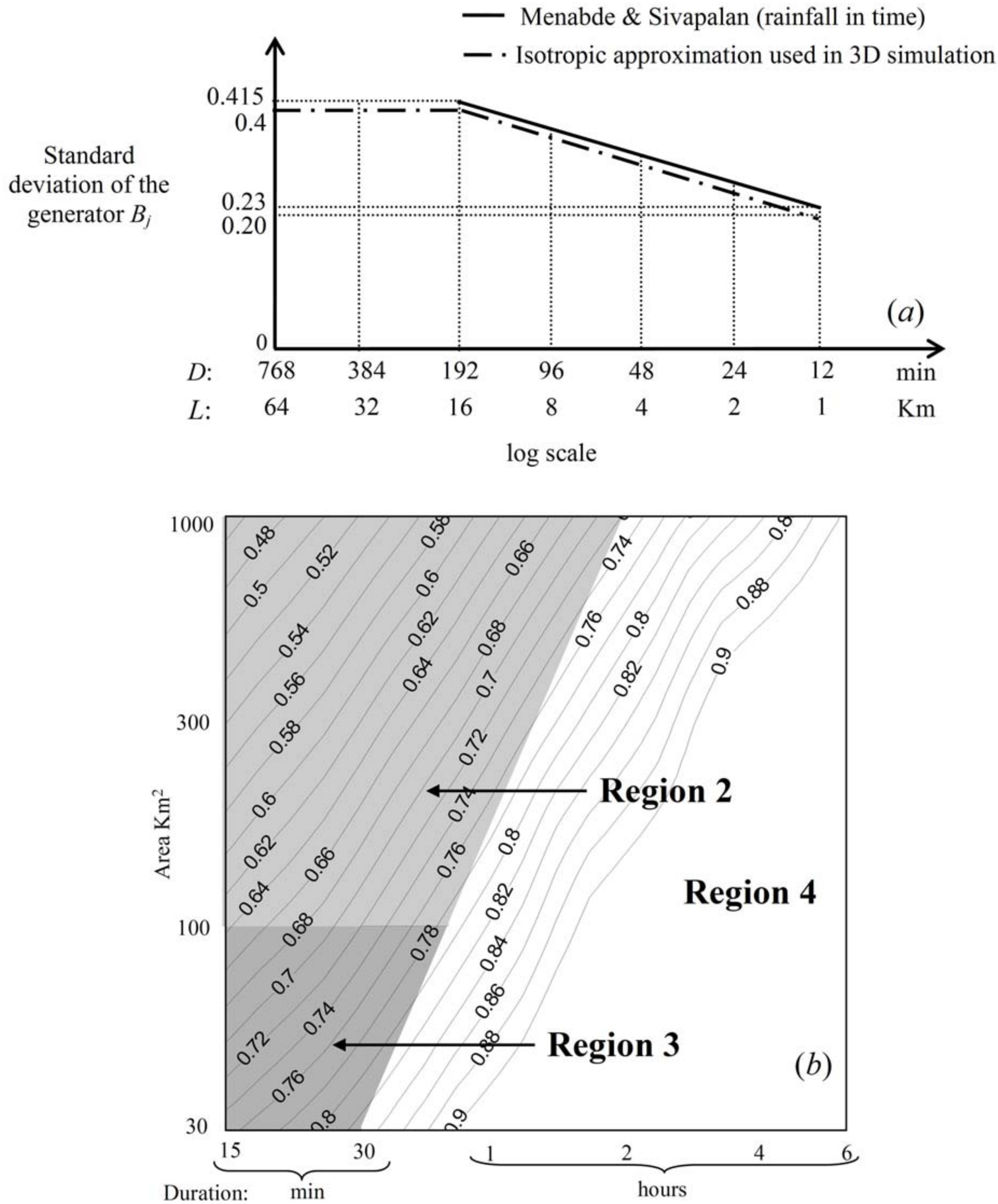

Figure 11: (*a*) Standard deviation of the bounded cascade generator used to produce the ARF values in (*b*). Rainfall is measured at points on a square grid with density of 1 raingauge per 4 Km^2.